

SUPPORTING INFORMATION

Support Functionalization to Retard Ostwald Ripening in Copper Methanol Synthesis Catalysts

Roy van den Berg¹, Tanja E. Parmentier¹, Christian F. Elkjær², Cedric J. Gommès³, Jens Sehested², Stig Helveg², Petra E. de Jongh¹, Krijn P. de Jong^{1*}

¹ Inorganic Chemistry and Catalysis, Debye Institute for Nanomaterials Science, Utrecht University, Universiteitsweg 99, 3584 CG Utrecht, Netherlands

² Haldor Topsoe A/S, Nymøllevej 55, DK-2800 Kgs. Lyngby, Denmark

³ Department of Chemical Engineering, University of Liège B6A, Allée du 6 août 3, B-4000 Liège, Belgium

* k.p.dejong@uu.nl

Overview.

1. Amine functionalization after copper deposition	2
Figure S1	
2. Effect of contact angle on Ostwald ripening	3
Figures S2-S4	
3. Measured contact angle	9
Table S1	
4. Electron Tomography	10
Figure S5	
5. Catalyst activity calculation	11
6. Cu/ZnO/Al₂O₃	13

Amine functionalization after copper deposition

Copper on silica (CS_2a) was functionalized with amine groups after copper deposition (CS_2a_N). The performance of both catalysts in the methanol synthesis reaction is shown in Figure S1. It can be seen that aminopropyl functionalization led to a stable performance over time. The activity of the catalyst had, however, decreased significantly. The loss in activity was probably due to blocking of the copper by the introduced amine groups.

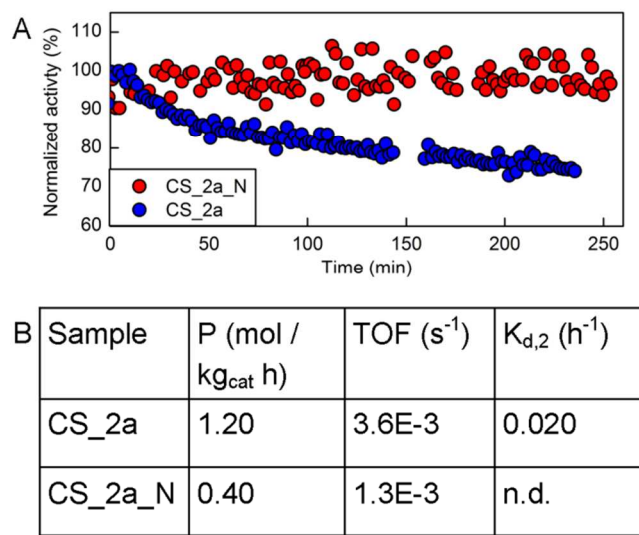


Figure S1. A) Normalized methanol synthesis activity over time for copper on silica (CS_2a, blue) and for a copper on silica functionalized after copper deposition (CS_2a_N, red). B) The initial productivity (P), initial turn over frequency (TOF) and deactivation constant (K_{d,2}) for CS_2a and CS_2a_N.

Effect of contact angle on Ostwald ripening

In the present section, we show that the observed changes in the deactivation rate are too large to be explained by the changes in the contact angles between the nanoparticles and the support. For that purpose, we assume that the overall rate of Ostwald ripening is proportional to the mass transfer between the smallest and the largest particles. We then calculate how that rate depends on the contact angle. Because our analysis overlooks screening and mean-field effects it provides an upper bound, which is sufficient for our present purpose. The typical shape of the nanoparticles is sketched in Fig. S2: we assume the particles to consist in a spherical cap having a radius of curvature R , and making an angle θ with the surface.

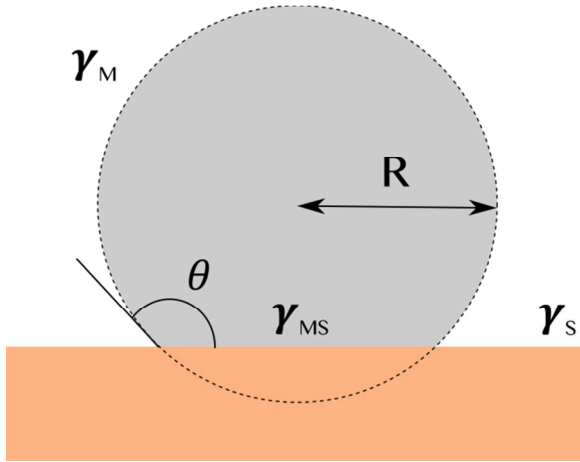


Figure S2. Sketch of a particle on a flat surface, with definition of the radius of curvature R , of the contact angle θ , as well as of the surface energies γ of the metal (M), support (S), and metal-support (MS) interfaces.

Using the standard formulae for the area and volume of spherical caps, one may express the volume V and free surface area A of the particle as follows as a function of the radius of curvature and of the contact angle.

$$V = \frac{4}{3} \pi R^3 f_V(\theta) \quad \text{Eq. 1}$$

and

$$A = 4 \pi R^2 f_A(\theta) \quad \text{Eq. 2}$$

The θ -dependent factors f_V and f_A can be seen as corrections compared to the spherical shape.

They are given explicitly by

$$f_V = \frac{1 - \cos(\theta)}{2} \left(1 - \cos(\theta) \frac{1 + \cos(\theta)}{2} \right) \quad \text{Eq. 3}$$

and

$$f_A = \frac{1 - \cos(\theta)}{2} \quad \text{Eq. 4}$$

Both functions are equal to one for the particular value $\theta = \pi$, which corresponds to a complete sphere.

Relation between a particle's apparent diameter and its radius of curvature

Analyzing TEM microscopy data with the geometrical model of Figure S2 is not straightforward because only the projections of the particles are measured. In particular, for a given radius of curvature R , the apparent diameter of the particle d depends on the value of θ .

The relation between d and R can be analyzed rigorously using Cauchy's relation between the surface area A of a 3D convex object and its average projected 2D area $A_{\text{projected}}$.

$$A_{\text{projected}} = A / 4 \quad \text{Eq. 5}$$

Where the average is calculated over all possible directions for the prognosis (Russ, J.C., Dehoff, R.T., "Practical stereology," second ed. Kluwer Academic, New York (2010)).

Defining the apparent diameter as the equivalent diameter of the projected area, $A_{\text{projected}} = \pi d^2/4$, Cauchy's formula can be particularized as

$$\pi \frac{d^2}{4} = \frac{1}{4} [4\pi R^2 f_A(\theta) + \pi R^2 \sin^2(\theta)] \quad \text{Eq. 6}$$

Where the first term in the brackets is the free area of the particle and the second term is the area in contact with the support. The relation can be written equivalently as

$$\frac{R}{d/2} = \left[1 - \left(\frac{1 + \cos(\theta)}{2} \right)^2 \right]^{-1/2} \quad \text{Eq. 7}$$

The relation between the apparent radius $d/2$ of the projected particles and their actual radius of curvature R is plotted in Fig. S3. The figure shows that projection biases are significant only for contact angles shallower than 90° . For contact angles larger than 135° , the effect is negligible, and we can therefore safely assume $R = d/2$.

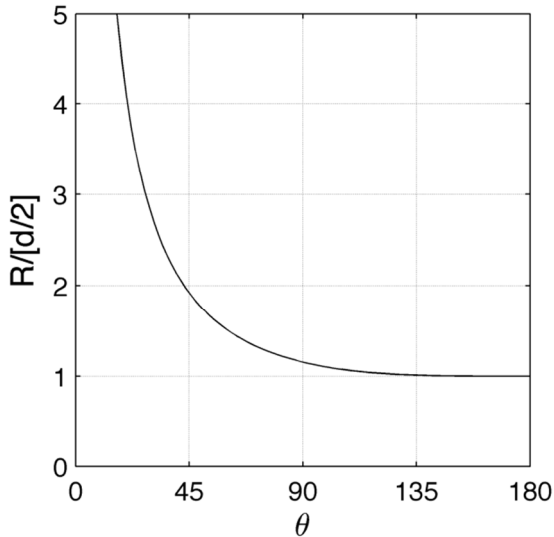


Figure S3. Relation between a particle's radius of curvature R and its apparent diameter d as a function of the contact angle θ .

Influence of the contact angle on Ostwald ripening

The main physicochemical characteristic of a nanoparticle for analyzing Ostwald ripening is its chemical potential μ , which controls the propensity of an atom to leave it or to condense on it.

The chemical potential is thermodynamically defined as $\mu = (\partial G / \partial N)$ where G is the free energy of the nanoparticle and N is the number of atoms it contains.

Because of the surface contributions to the free energy, the chemical potential of a nanoparticle is generally size-dependent. In the case of a supported nanoparticle, as in Figure S2, Gibbs relation writes

$$dG = \mu_0 dN + \gamma_M dA + \gamma_S dA_S + \gamma_{MS} dA_{MS} \quad \text{Eq. 8}$$

where μ_0 is the chemical potential of the bulk (i.e. macroscopic) material, A is the area of the particle's free surface, A_S is the area of the support, and A_{MS} is the area of the metal-support interface. The latter area can be expressed as

$$A_{MS} = \pi R^2 \sin^2(\theta) \quad \text{Eq. 9}$$

and the change in area of the free surface of the support satisfies $dA_S + dA_{MS} = 0$. Taking also into account that the surface energies are related to the contact angle via the Young-Duprez relation

$$\gamma_M \cos(\theta) = \gamma_S - \gamma_{MS} \quad \text{Eq. 10}$$

one eventually finds the simple relation

$$\mu = \left(\frac{\partial G}{\partial N} \right) = \mu_0 + \frac{2\gamma_M \Omega}{R} \quad \text{Eq. 11}$$

where Ω is the volume occupied by an atom in the nanoparticle.

Eq. 11 is identical to the case of a spherical nanoparticle, only R is here the radius of curvature, which for a given particle volume V depends on the contact angle θ via Eq. 1.

The solubility of a material or the partial pressure of a vapor in equilibrium with it scales with its chemical potential as

$$c_{eq} \propto \exp\left(\frac{\mu}{k_B T}\right) \quad \text{Eq. 12}$$

Where k_B is Boltzmann's constant and T is the temperature. Assuming that Ostwald ripening is limited by the diffusion of species from small nanoparticles to larger ones, the overall rate of the process can therefore be estimated as the difference between Eq. 12 estimated for the smallest and for the largest values of R .

The contact-angle dependence of c_{eq} for two particles having the same volumes as spheres with diameter 4 nm and 2 nm are plotted in Figure S4a. These curves were obtained by combining Eq. 11 and 12 with $\lambda = \gamma_M \Omega / k_B T = 5.28$ nm. The latter value corresponds to Cu at $T = 260$ °C. The values of c_{eq} converge to the bulk equilibrium concentration for extremely shallow contact angles because the metal surface is almost flat in that limit.

When everything else is kept constant, the rate of diffusion between the small and the large nanoparticles considered in Fig. S4a, scales like the difference of the two concentrations. The corresponding values are plotted in Fig. S4b. This figure therefore shows that experimentally observed changes in contact angle (see Table S1) would result in changes of only about 10% of the rate of Ostwald ripening. The change in contact angle can thus not explain the 3-fold faster deactivation for the non-functionalized sample.

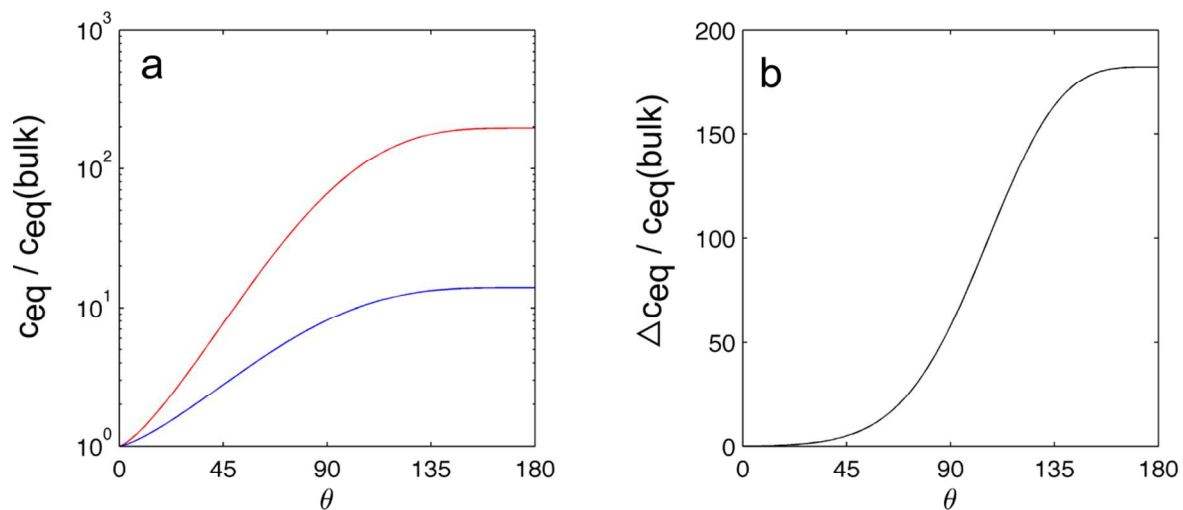


Figure S4. (a) Contact-angle dependence of the equilibrium vapor concentrations of two nanoparticles having the same volume as spheres with diameter 4 nm (blue) and 2 nm (red). (b) Difference of the two concentrations, proportional to the rate of diffusion between the two particles. In both graphs, the concentrations are normalized by the bulk value, corresponding to a flat interface (i.e. $\theta = 0$)

Measured contact angle

The contact angle of copper on silica and on amine-functionalized silica, determined with *in-situ* TEM, was measured in two ways. If particles were imaged (almost) edge on, the contact angle was measured directly. The directly measured contact angles set the lower value of the real contact angle since the observed contact angle is lower if the particle is not perfectly imaged edge on. If particles were imaged close to edge on, the contact angle was also determined via the height (h) / width (w) ratio. The formula used to calculate the contact angle (θ) was:

$$\theta = 180 - \cos^{-1}\left(\frac{h - \frac{w}{2}}{\frac{w}{2}}\right) \quad \text{Eq. 13}$$

With this method the determined contact angle is larger than the real contact angle if the particle is not perfectly imaged edge on. The real contact angle was estimated by averaging the contact angles obtained via both methods (Table S1). No dependence of the contact angle upon the particle size (2-5 nm) was found.

Table S1. Contact angles determined via the direct and indirect method for both samples.

Sample	Direct θ	Counts	Indirect θ (h/w)	Counts	Average θ
CS_1a	130 ± 24	23	141 ± 14	33	135
CSN_1b	116 ± 18	14	135 ± 16	23	125

Electron Tomography

Electron tomography was performed on CS_2a after reduction on a Tecnai 20 (FEI) transmission electron microscope at a primary electron energy of 200 kV in bright-field imaging mode. Copper grids with parallel bars and carbon films with thin areas of just 2 nm in thickness were used. These grids were wetted with a solution of 5 nm colloidal gold particles and subsequently dried. These gold particles acted as fiducial markers during the alignment. The catalyst sample was dispersed in ethanol and subsequently deposited on the copper grids. Tilt images were recorded from -70° to $+70^\circ$ with intervals of 2 degrees. The resulting images were aligned to a common origin and rotation axis by tracking the 5 nm Au fiducial markers. 3D reconstruction was performed on these tilt series using a weighted back-projection algorithm in IMOD (J.R. Kremer, D.N. Mastronarde, J.R. McIntosh, *Journal of Structural Biology*, 116 (1996) 71-76.).

In the electron tomogram section of CS_2a after reduction in Figure S5 it can be seen that the silica primary particles were partly fused together forming larger aggregates. Moreover, a few 2-3 nm sized copper particles located on the silica (darker image features) are visible.

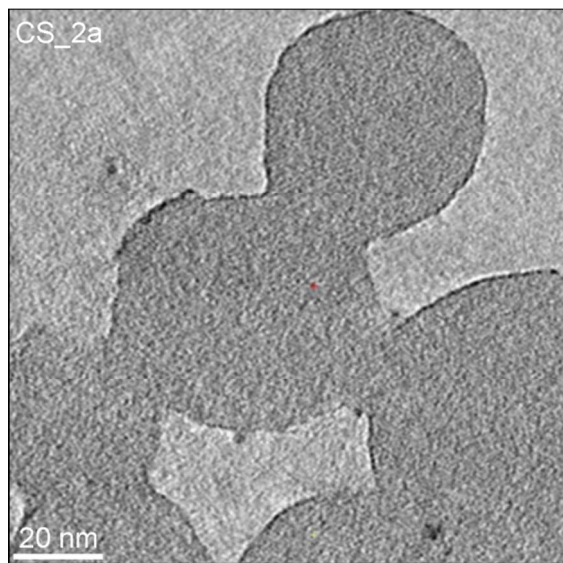


Figure S5. Electron tomogram section (0.52 nm in thickness) of CS_2a after reduction.

Catalyst activity calculation

The methanol productivity is based upon the CO + CO₂ conversion. The conversion of CO or CO₂ is calculated by the difference in CO/Ar or CO₂/Ar ratio between chromatograms taken during reaction and chromatograms taken of the gas feed before reaction (eq. 14 and 15).

$$X_{CO} = \frac{\frac{CO_{feed}}{Ar_{feed}} - \frac{CO_{reaction}}{Ar_{reaction}}}{\frac{CO_{feed}}{Ar_{feed}}} \quad \text{Eq. 14}$$

$$X_{CO_2} = \frac{\frac{CO_2_{feed}}{Ar_{feed}} - \frac{CO_2_{reaction}}{Ar_{reaction}}}{\frac{CO_2_{feed}}{Ar_{feed}}} \quad \text{Eq. 15}$$

X_{CO} and X_{CO₂} are the conversion of CO and CO₂, respectively. CO_{feed}, CO₂_{feed} and Ar_{feed} are the peak areas of the corresponding gases in the TCD chromatograms of the syngas feed before catalysis. CO_{reaction}, CO₂_{reaction} and Ar_{reaction} are the peak areas of the exit gas composition during catalysis. The methanol productivity is calculated by the CO + CO₂ conversion (eq. 16).

$$n_{MeOH} = X_{CO} * n_{CO} + X_{CO_2} * n_{CO_2} \quad \text{Eq.16}$$

n_{MeOH} is the rate of methanol production. n_{CO} or n_{CO₂} is the molar flow rate of CO or CO₂, respectively, into the reactor, calculated via equation 17 and 18.

$$n_{CO} = \frac{Q_{CO} * P_{ref}}{RT_{ref}} * \phi \quad \text{Eq.17}$$

$$n_{CO_2} = \frac{Q_{CO_2} * P_{ref}}{RT_{ref}} * \phi \quad \text{Eq. 18}$$

Q_{CO} or Q_{CO₂} are the molar fractions of CO and CO₂ in the syngas feed, P_{ref} is the pressure and T_{ref} the temperature at which the mass flow controller has been calibrated and R is the gas constant. ϕ is the syngas flow into the reactor as measured by the mass flow controller. To obtain catalyst mass-based productivities (P) The calculated rate of methanol production was divided by the mass of the catalyst (m_{cat}) according to Eq. 19.

$$P = \frac{n_{MeOH}}{m_{cat}} \quad \text{Eq. 19}$$

Turn over frequencies (TOF) were calculated with the assumption that each copper surface atom was an active site. The number of copper surface atoms was based on the TEM particle size distributions assuming fully accessible spherical particles. First, the surface averaged particle size (PS) was calculated via Eq. 20.

$$PS = \frac{\sum_1^n D_i^3}{\sum_1^n D_i^2} \quad \text{Eq. 20}$$

D_i is the diameter of the i th particle. The dispersion (ratio between copper surface atoms and total copper atoms) was calculated according to Eq. 21.

$$dispersion = \frac{6V_m}{A_m * PS} \quad \text{Eq. 21}$$

V_m is the molar volume and A_m the molar area of the particles. In the case of copper V_m is $7.09 * 10^{21} \text{ nm}^3$ and A_m is $4.10 * 10^{22} \text{ nm}^2$. The dispersion of copper ($dispersion_{cu}$) is therefore given by Eq. 22 with PS in nm.

$$dispersion_{cu} = \frac{1.04}{PS} \quad \text{Eq. 22}$$

The molar amount of copper surface atoms in the catalyst (Cu_{surf}) was calculated by Eq. 23

$$Cu_{surf} = dispersion_{cu} * \frac{Wt_{cu}}{M_{cu}} * m_{cat} \quad \text{Eq. 23}$$

Where Wt_{cu} is the weight fraction of copper in the catalyst and M_{cu} the molar mass of copper.

TOFs were calculated according to Eq. 24

$$TOF = \frac{n_{MeOH}}{Cu_{surf}} \quad \text{Eq. 24}$$

Cu/ZnO/Al₂O₃

The reference Cu/ZnO/Al₂O₃ catalyst was prepared by co-precipitation. 30 ml of a 1M aqueous solution of Cu and Zn and Al nitrates (55:30:15 atomic ratio) was added dropwise (2 ml min⁻¹) to 50 ml of deionized water kept at 338 K for which the pH had been previously adjusted to 7.0 with Na₂CO₃. Simultaneously 1.5 M Na₂CO₃ solution was added at a controlled rate over a period of 15 minutes in order to keep the pH at 7 ± 0.1. The obtained precipitate was aged for 2 h at 338 K in the mother liquor under vigorous stirring, filtrated, extensively washed with water, dried at 343 K and calcined at 673 K in a muffle oven. Catalytic testing was performed at the same conditions as the (functionalized) Cu/SiO₂ catalysts. For this, 0.06 g Cu/ZnO/Al₂O₃ was diluted with SiC in a SiC:catalyst volume ratio of 4:1. The syngas flow was adjusted to obtain CO conversion levels near 20%.